

Quantum computation of dominant products in lithium-sulfur batteries

Julia E. Rice,^{1, a)} Tanvi P. Gujarati,¹ Mario Motta,¹ Tyler Y. Takeshita,² Eunseok Lee,² Joseph A. Latone,¹ and Jeannette M. Garcia¹

¹⁾IBM Quantum, Almaden Research Center, San Jose, CA 95120, USA

²⁾Mercedes Benz Research and Development North America, Sunnyvale, CA 94085, USA

Quantum chemistry simulations of some industrially relevant molecules are reported, employing variational quantum algorithms for near-term quantum devices. The energies and dipole moments are calculated along the dissociation curves for lithium hydride (LiH), hydrogen sulfide (H₂S), lithium hydrogen sulfide (LiSH) and lithium sulfide (Li₂S). In all cases we focus on the breaking of a single bond, to obtain information about the stability of the molecular species being investigated. We calculate energies and a variety of electrostatic properties of these molecules using classical simulators of quantum devices, with up to 21 qubits for lithium sulfide. Moreover, we calculate the ground-state energy and dipole moment along the dissociation pathway of LiH using IBM quantum devices. This is the first example, to the best of our knowledge, of dipole moment calculations being performed on quantum hardware.

INTRODUCTION

Lithium-sulfur batteries are a promising next-generation battery technology with a high theoretical capacity of up to ~1675 mAh/g and a high theoretical energy density of ~2600 Wh/kg (Li-ion theoretical energy density is ~350-500 Wh/kg)¹⁻⁶. The reversible battery functioning is based on the electrochemistry between lithium metal (Li⁰) and elemental sulfur (S₈) to form lithium sulfide (Li₂S) as the thermodynamic product, illustrated in Figure 1. The reduction of sulfur is known to proceed on discharge in the battery, through a series of intermediate lithium polysulfide salts, some of which are soluble in the electrolyte and can diffuse to the lithium metal anode⁷⁻¹¹. The solubility of various intermediates provides unique challenges for the realization of lithium-sulfur

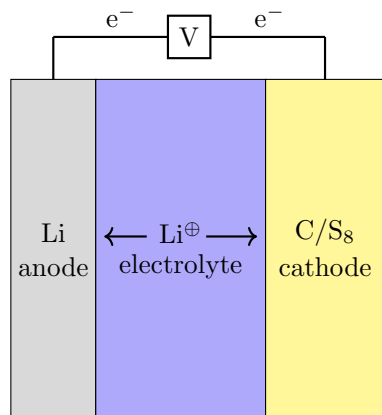


FIG. 1. Schematic representation of a lithium-sulfur battery. During discharge, elemental sulfur is reduced into sulfur salts containing chains of varying lengths, ultimately resulting in lithium sulfide production. During charge, the chemistry is reversed. The mechanism for lithium sulfide production is proposed to occur through a two-electron process.

batteries and limits the potential use of lithium-sulfur as a practical alternative to state-of-the-art lithium-ion^{12,13}.

In order to harness control over the battery technology, the mechanism for production and identification of reactive intermediates must be validated. However, the reaction mechanism for sulfur reduction in the battery environment is highly complex and debated in the field. Intermediates are difficult (if not impossible) to characterize during operation of the battery and competing chemical (vs electrochemical) pathways are also active, which confounds the mixture of products produced. Generally, products are assumed to be produced through either one electron or two electron processes, which generate radicals and Li-S salts, in which the sulfur anion consists of 1-8 sulfur atoms. Four electron processes have also been considered but are unlikely as there is little experimental evidence and for entropic reasons¹⁴.

The molecular electron-density distribution and, in particular, the resulting dipole moment, are critical for understanding a variety of phenomena occurring in batteries. In general, molecules with high polarity can easily attract or repel valence electrons from other compounds and generate reactions through electron transfer. The dipole moment of a molecule also determines its response to an external electric field. Accurate computation of energetics and dipole moments of molecules is thus a problem with deep conceptual importance, and significant applicability to the chemistry of LiS batteries. Achieving this goal requires solving the Schrödinger equation for the molecules of interest, a problem that is known to be exponentially expensive for classical computers unless approximation schemes are introduced.

Quantum computing is an alternative and complementary mode of attack of mathematical problems, that has significant potential to provide advantage over conventional computing in a number of areas, including simulation of Hamiltonian dynamics¹⁵⁻¹⁸. A number of heuristics to provide approximate but highly accurate solutions to the Schrödinger equation have been proposed, in particular the Variational Quantum Eigensolver (VQE)¹⁹⁻²¹. Over the last years, researchers have demonstrated the use and accuracy of VQE in investigations of a variety of molecules^{19,20,22-29}.

Motivated by these results, and by the importance of computing energies and electrostatic properties, in this work we assess the performance of quantum algorithms in determining

^{a)}corresponding author, jrice@us.ibm.com

ground state energies and dipole moments along bond stretching for LiH, H₂S, LiSH and Li₂S, using classical simulators of quantum devices. The calculations presented here are important for the development of quantum computing: to the best of our knowledge, we present the first quantum hardware results of dipole moments, focusing on the LiH molecule. Our results immediately generalize to expectation values of k -body operators in materials, with significant implications for the ability to study reactivity and electrostatics in batteries by quantum algorithms.

METHODOLOGY

A. Working equations

The overall strategy for the calculations performed in this work involved initial pre-processing by classical quantum chemistry codes on conventional computers, to generate optimized Hartree-Fock orbitals and matrix elements of the Hamiltonian, prior to performing computations with quantum simulators or devices. The restricted Hartree-Fock (RHF) singlet state has been chosen as the initial state for all of the calculations described here, since experience has indicated this state as a good choice for a variety of chemical problems³⁰. Restricted coupled-cluster with singles and doubles (CCSD) and full configuration interaction (FCI) calculations were performed using Psi4³¹, at STO-3G level of theory, using the frozen-core approximation for correlated calculations. The choice of the minimal basis is motivated by the fact that only a few molecular orbitals can be described on contemporary quantum hardware, since the number of available qubits is still relatively small, devices are noisy, and full quantum error correction techniques are not yet available. Additional details for the studied molecules are listed in the Supplementary Material.

Having selected a set of single-electron orbitals for each of the studied species, VQE computations were performed with quantum simulators and devices. Achieving this goal requires first defining a Hilbert space \mathcal{H} spanned by $2n$ orthonormal one-electron wavefunctions $\{\phi_p \otimes \chi_\sigma\}_{p\sigma}$, where $\{\phi_p\}_{p=1}^n$ are a set of orthonormal spatial orbitals, here RHF orbitals, and χ_σ are spin- z eigenfunctions, with $\sigma = \uparrow, \downarrow$.

For each of the $2n$ spin-orbitals $\phi_p \otimes \chi_\sigma$, we then define a creation operator $\hat{c}_{p\sigma}^\dagger$, and construct the fermionic Fock space \mathcal{F} . Now, \mathcal{F} is of course a 2^{2n} -dimensional Hilbert space, which is very naturally mapped³²⁻³⁴ onto the Hilbert space of $m = 2n$ qubits. An important example of such a mapping is the Jordan-Wigner transformation

$$\begin{aligned} \hat{c}_{p\uparrow}^\dagger &\mapsto \frac{X_p - iY_p}{2} Z_0^{p-1}, \\ \hat{c}_{p\downarrow}^\dagger &\mapsto \frac{X_{n+p} - iY_{n+p}}{2} Z_0^{n+p-1}, \\ \hat{c}_{p\uparrow} &\mapsto \frac{X_p + iY_p}{2} Z_0^{p-1}, \\ \hat{c}_{p\downarrow} &\mapsto \frac{X_{n+p} + iY_{n+p}}{2} Z_0^{n+p-1}, \end{aligned} \quad (1)$$

with $Z_s' = Z_r Z_{r-1} \dots Z_{s+1} Z_s$. Of course there exist several alternatives, most notably the parity and Bravyi-Kitaev encod-

ings, that can be combined with ‘‘tapering’’ techniques to reduce the number m of qubits leveraging conservation of particle number modulo 2 and the presence of \mathbb{Z}_2 symmetries of molecular orbitals³³⁻³⁹. When fermionic wavefunctions can be mapped onto m -qubit wavefunctions, fermionic k -body operators are mapped onto linear combination of Pauli operators acting on m qubits,

$$\sum_{\substack{p_1 \dots p_k \\ q_1 \dots q_k}} O_{q_1 \dots q_k}^{p_1 \dots p_k} \hat{E}_{p_1 \dots p_k}^{q_1 \dots q_k} \mapsto \sum_i c_i P_i, \quad (2)$$

where $P_i \in \{\mathbb{1}, X, Y, Z\}^{\otimes m}$ is an m -qubit Pauli operator, and

$$\hat{E}_{p_1 \dots p_k}^{q_1 \dots q_k} = \sum_{\sigma_1 \dots \sigma_k} \hat{c}_{p_1 \sigma_1}^\dagger \dots \hat{c}_{p_k \sigma_k}^\dagger \hat{c}_{q_k \sigma_k} \dots \hat{c}_{q_1 \sigma_1} \quad (3)$$

is a spin-summed k -body excitation operator. For example, under Jordan-Wigner representation, one-body operators $\hat{O} = \sum_{pq} O_q^p \hat{E}_p^q$ transform onto

$$\begin{aligned} \hat{O} &\mapsto \sum_p O_p^p \frac{\mathbb{1} - Z_p}{2} + \sum_p O_p^p \frac{\mathbb{1} - Z_{n+p}}{2} \\ &+ \sum_{p < q} O_q^p \frac{X_q Z_{p+1}^{q-1} X_p + Y_q Z_{p+1}^{q-1} Y_p}{2} \\ &+ \sum_{p < q} O_q^p \frac{X_{n+q} Z_{n+p+1}^{n+q-1} X_{n+p} + Y_{n+q} Z_{n+p+1}^{n+q-1} Y_{n+p}}{2} \end{aligned} \quad (4)$$

Once k -body operators are encoded onto qubit operators, they can of course be measured, using standard techniques, on a register of qubits prepared in a suitable wavefunction. In this work, to produce an accurate approximation for the ground state of the system, we use the VQE algorithm, in which a parametrized quantum circuit $\hat{U}(\theta)|\Psi_0\rangle$ is used to correlate an initial mean-field wavefunction Ψ_0 , corresponding to the RHF state, and the best approximation to the ground state is determined by numerically minimizing the energy $E(\theta) = \langle \Psi_0 | \hat{U}(\theta)^\dagger \hat{H} \hat{U}(\theta) | \Psi_0 \rangle$. Once the optimal parameters are found, properties can be evaluated as expectation values of suitable qubit operators over the VQE wavefunction.

Here, we focused on multipole moments, which we evaluate as expectation values of one-body operators,

$$M^{i_1 \dots i_n} = M_n^{i_1 \dots i_n} - \langle \Psi | \hat{M}_e^{i_1 \dots i_n} | \Psi \rangle \quad (5)$$

given by a nuclear and an electronic contributions,

$$\begin{aligned} M_n^{i_1 \dots i_n} &= \sum_\alpha Z_\alpha R_\alpha^{i_1} \dots R_\alpha^{i_n} \\ \hat{M}_e^{i_1 \dots i_n} &= \sum_{pq} (M^{i_1 \dots i_n})_q^p \hat{E}_p^q \\ (M^{i_1 \dots i_n})_q^p &= \int d^3 \mathbf{r} r^{i_1} \dots r^{i_n} \phi_p(\mathbf{r}) \phi_q(\mathbf{r}) \end{aligned} \quad (6)$$

respectively, where $i_1 \dots i_n = x, y, z$ are indices labeling Cartesian components, and Z_α, R_α are the atomic numbers and the positions of the nuclei respectively.

From the quantities $M^{i_1 \dots i_n}$, we easily obtain the dipole, quadrupole, octopole and hexadecapole moments in the traceless Buckingham expansion⁴⁰⁻⁴⁴, respectively defined as

$$\begin{aligned}
\mu^a &= M^a \\
\Theta^{ab} &= \frac{1}{2!} \left[3M^{ab} - M^{kk} \delta^{ab} \right] \\
\Omega^{abc} &= \frac{1}{3!} \left[15M^{abc} - 3(M^{akk} \delta^{bc} + M^{kbb} \delta^{ac} + M^{kkc} \delta^{ab}) \right] \\
\Phi^{abcd} &= \frac{1}{4!} \left[105M^{abcd} - 15(M^{abkk} \delta^{cd} + M^{akck} \delta^{bd} + M^{akkd} \delta^{bc} + M^{kbck} \delta^{ad} + M^{kbbd} \delta^{ac} + M^{kkcd} \delta^{ab}) \right. \\
&\quad \left. + 3(M^{kkll} \delta^{ab} \delta^{cd} + M^{klkl} \delta^{ac} \delta^{bd} + M^{kllk} \delta^{ad} \delta^{bc}) \right],
\end{aligned} \tag{7}$$

where repeated indices ($k, l = x, y, z$) are summed over. Multipole moments are converted to spherical molecular moments as detailed in Table E1 of Ref [40].

We evaluate the charge density and molecular electrostatic potential, respectively defined as

$$\rho(\mathbf{r}) = \sum_{pq} \phi_p(\mathbf{r}) \phi_q(\mathbf{r}) \langle \Psi | \hat{E}_p^q | \Psi \rangle \tag{8}$$

and

$$\begin{aligned}
V(\mathbf{r}) &= V_n(\mathbf{r}) - V_e(\mathbf{r}), \\
V_n(\mathbf{r}) &= \sum_{\alpha} \frac{Z_{\alpha}}{\|\mathbf{r} - \mathbf{R}_{\alpha}\|}, \\
V_e(\mathbf{r}) &= \int d^3\mathbf{r}' \frac{\rho(\mathbf{r}')}{\|\mathbf{r} - \mathbf{r}'\|} = \sum_{pq} V_{pq} \langle \Psi | \hat{E}_p^q | \Psi \rangle
\end{aligned} \tag{9}$$

In this work, we elected to evaluate multipole moments as expectation values of one-body operators. There exists of course an alternative approach, based on the definition of the dipole moment as the derivative of the ground-state energy with respect to an external electric field^{45–51}.

Within such an approach, the dipole moment definition includes additional terms that depend on the derivatives of the Hartree-Fock orbitals with respect to the external electric field.

The strategy of computing dipole moments as expectation values of one-body operators is simpler and more economical, as it requires $\mathcal{O}(n^3)$ rather than $\mathcal{O}(n^5)$ measurements of Pauli operators when the Jordan-Wigner encoding is used. Moreover, it does not require calculating energies within sub-milli-Hartree statistical accuracy, making it suitable for contemporary quantum hardware.

The implementation and hardware demonstration of gradient-based approaches is a valuable direction of research in the development and refinement of experiments on quantum hardware^{52–56}, especially important in the investigation of second-order derivatives, such as polarizabilities and shielding tensors.

We defined the charge density and electrostatic potential in terms of the spin-summed one-body density matrix $\langle \Psi | \hat{E}_p^q | \Psi \rangle$ (1RDM) because, unlike multipole moments, these quantities are evaluated on very large meshes of spatial points. Therefore, they are more conveniently computed by measuring and post-processing the 1RDM. Multipole moments, on the other hand, are more naturally evaluated as expectation values of hermitian operators, without extracting and post-processing the 1RDM.

B. Computational details

We use IBM's open-source Python library for quantum computing, Qiskit⁵⁷. Qiskit provides tools for various tasks such as creating quantum circuits, performing simulations, and computations on real hardware. It also contains an implementation of the VQE algorithm, a hybrid quantum-classical algorithm that uses both quantum and classical resources to solve the Schrödinger equation and a classical exact eigen-solver algorithm to compare results.

In the VQE algorithm, we take our wavefunction in the form of a quantum circuit, which is the unitary coupled cluster with singles and doubles (UCCSD)^{58–60}, its quantum variant (q-UCCSD) as defined in Ref [61], and the following Ry Ansatz,

$$|\Psi(\theta)\rangle = \prod_{k=1}^{n_r} \left(\prod_{i=0}^{m-1} R_{y,i}(\theta_{k,i}) \prod_{ij \in C} G_{ij} \right) \prod_{i=0}^{m-1} R_{y,i}(\theta_{0,i}) |\Psi_0\rangle, \tag{10}$$

where $|\Psi_0\rangle$ is an initial wavefunction (here, the restricted closed-shell Hartree-Fock state), m is the number of qubits, $R_{y,i}(\theta) = \exp(-i\theta Y_i/2)$ is a Y rotation of an angle θ applied to qubit i , G_{ij} a parameter-free two-qubit entangling gate (here, the CNOT gate) applied to a pair (ij) of connected qubits (here, we chose linear connectivity, i.e. $(ij) \in C$ if and only if $j = i + 1$), and n_r is an integer denoting the number of times a layer of entangling gates followed by a layer of Y rotations is repeated.

We then minimize the expectation value of the Hamiltonian with respect to the parameters of our circuit. The minimization is carried out through the classical optimization method, L_BFGS_B^{62–64} on the simulator, and Simultaneous Perturbation Stochastic Approximation (SPSA)^{65,66} on the device. Once the VQE is complete, we obtain the optimized variational form and the estimate for the ground state energy. In addition, we measure the one-body operators corresponding to the components of the dipole, quadrupole, octopole and hexadecapole moments, and the electron density and electrostatic potential from the spin-summed one-particle density matrix $\langle \Psi | \hat{E}_p^q | \Psi \rangle$.

We chose molecular geometries to lie in the xz plane of a suitable frame of reference, with the center of mass occupying the origin of such a frame of reference, and the heaviest element having $z < 0$.

We ran our experiments on both the statevector and qasm simulators in Qiskit. We performed hardware experiments

on 5 qubit devices available through IBM Quantum Experience each with Quantum Volume⁶⁷ of 32, namely, *ibmq_rome*, *ibmq_athens*, *ibmq_bogota* and *ibmq_santiago*⁶⁸. We employed readout-error mitigation^{69–71} as implemented in Qiskit Ignis to correct measurement errors. We also used a simple noise extrapolation scheme using additional CNOT gates at the minimum energy VQE iterations to account for errors introduced during the expensive 2-qubit entangling operations as was shown in Refs [72, 73].

RESULTS AND DISCUSSION

C. Quantum computation of lithium-sulfur molecules

The stability of Li_2S in batteries is related to the amount of energy needed to break one Li–S bond. So, in this study, we have studied the dissociation of one bond, rather than two bonds simultaneously.

1. Lithium hydride (LiH)

After removing the frozen core orbital (Li 1s), the lithium hydride (LiH) bond can be represented by molecular (spatial) orbitals (MOs) with 2s, 2p_z character for lithium (since LiH is placed along the z axis) and an MO with 1s character for hydrogen, for a total of 6 spin-orbitals. The ground state energy and dipole moment norm were calculated over a range of bond distances on the simulator and on the hardware through

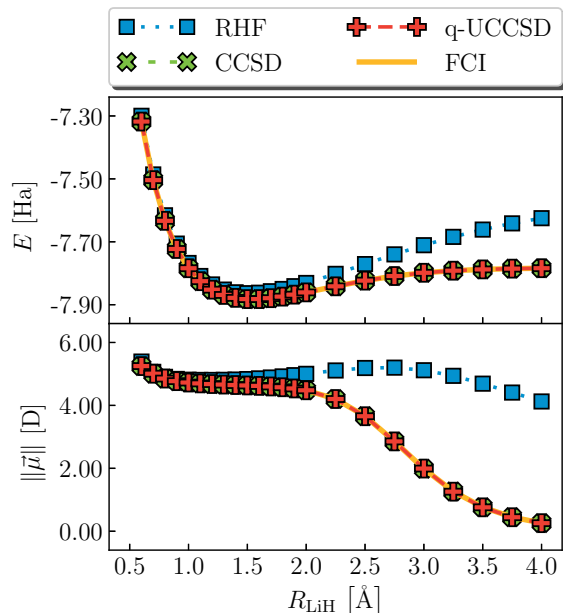


FIG. 2. Calculations for lithium hydride, LiH. Top: Dissociation curve (ground state energy in Hartrees) as a function of interatomic distance (in Angstroms) from RHF, CCSD, q-UCCSD and FCI. Bottom: Dipole moment (in Debye) as a function of interatomic distance (in Angstroms).

the use of four qubits after tapering³⁷ techniques were applied.

As seen in Figure 2, results from CCSD and FCI coincide for both energy and dipole moment along bond stretching, since these methods are equivalent for two-electron systems. Also q-UCCSD values are essentially the same as FCI. Despite its simplicity, LiH has an interesting evolution in the dipole moment along the dissociation curve from a regime with ionic character (polar, short R_{LiH} , $\|\vec{\mu}\| \simeq 4.6$ D) to one without polarity (large R_{LiH} , $\|\vec{\mu}\| \simeq 0$). The large change in the dipole moment between 2.0 and 3.5 Å correlates with the pronounced deviation of the energy dissociation curve from that of the FCI in the first results reported on quantum hardware, see Figure 3 of Ref [20]. Both of these observations are consistent with the fact that there is more entanglement/electron correlation across this bond length range, and thus higher circuit depth is needed.

2. Hydrogen sulfide (H_2S)

After removing frozen core orbitals, hydrogen sulfide (H_2S) is represented by MOs with 3s, 3p_x, 3p_y, 3p_z character for sulfur and an MO with 1s character for hydrogen, totaling 12 spin orbitals and 8 electrons. Upon employing tapering and associated qubit reductions to exploit symmetries in the molecule^{37,74}, the q-UCCSD ground state energy and dipole moment norm were calculated over a range of bond distances on the simulator with 9 qubits as illustrated in Figure 3. Also plotted are the corresponding CCSD and FCI energies and dipole moment norms.

q-UCCSD and CCSD are in agreement with the FCI energies across bond stretching (the maximum deviation in milli-Hartrees from the FCI value being 0.085 (at 2.15 Å) and 0.131 (at 2.15 Å) respectively, with q-UCCSD providing a better estimate of the energy for large R_{HS} . Note that the the CCSD energy actually goes below the FCI value at large R_{HS} , a known deficiency of CCSD to describe the molecular energy when the bond length is far from the equilibrium value.

The dipole moment norm is seen to monotonically decrease with R_{HS} towards ~ 0.67 D, which is the dipole moment norm of the HS fragment, and again q-UCCSD values are in better agreement with FCI than CCSD ones (the maximum deviations from FCI being 2 milliDebye and 12 milliDebye respectively).

As seen in Figure 3, differences between q-UCCSD and FCI energies are always greater than zero. This can be understood, since the q-UCCSD energies are variational in nature^{58–60} but since the method only includes single and double excitations, the values must lie above the FCI values. It is also understandable that the most challenging regime is the intermediate dissociation regime ($R_{\text{HS}} \simeq 1.8$ Å) where the ground-state wavefunction is switching between different dominant determinants in its configuration interaction expansion, exhibiting multi-reference character.

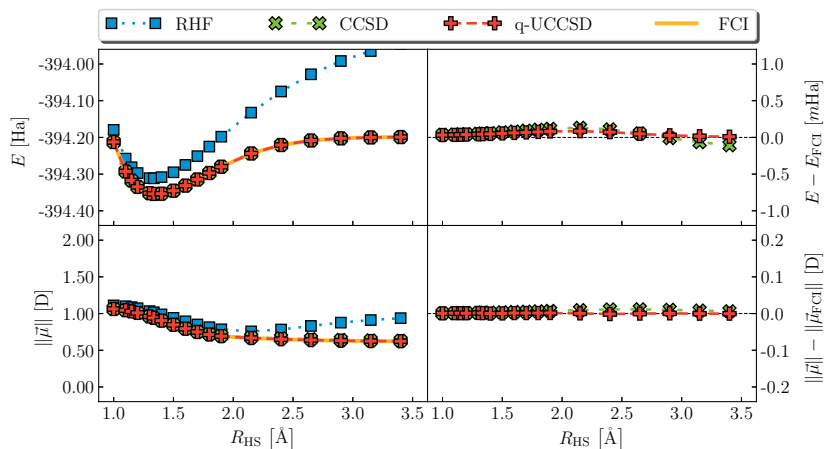


FIG. 3. Calculations for H_2S . Top left: dissociation curve as a function of HS distance from RHF, CCSD, q-UCCSD and FCI. Top right: Deviation from FCI energy, for CCSD and q-UCCSD. Bottom left: norm of the dipole moment as a function of HS distance. Bottom right: deviation from FCI dipole, for CCSD and q-UCCSD.

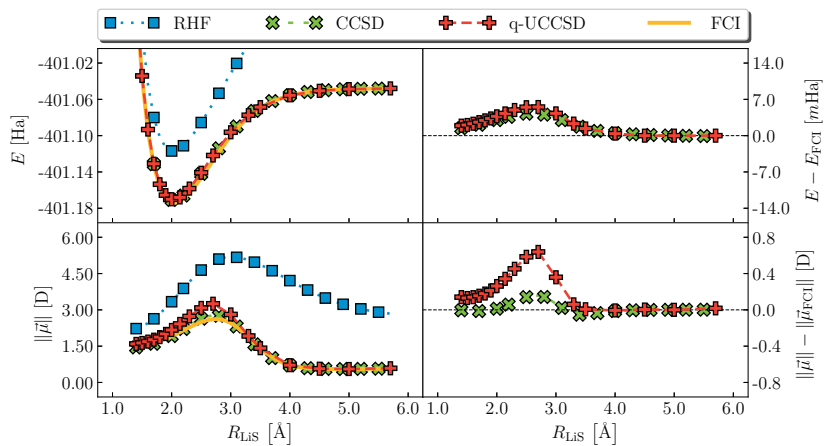


FIG. 4. Calculations for LiSH , when breaking the Li-S bond. Top left: dissociation curve as a function of LiS distance from RHF, CCSD, q-UCCSD and FCI. Top right: Deviation from FCI energy, for CCSD and q-UCCSD. Bottom left: norm of the dipole moment as a function of LiS distance. Bottom right: deviation from FCI dipole, for CCSD and q-UCCSD.

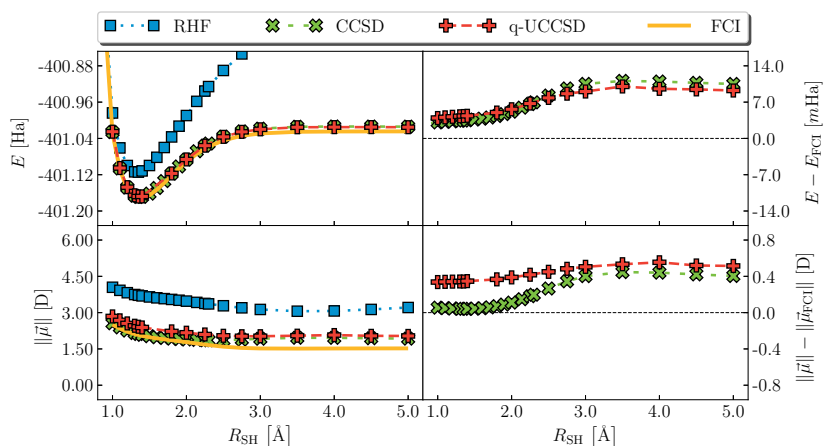


FIG. 5. Calculations for LiSH , when breaking the H-S bond. Top left: dissociation curve as a function of HS distance from RHF, CCSD, q-UCCSD and FCI. Top right: Deviation from FCI energy, for CCSD and q-UCCSD. Bottom left: norm of the dipole moment as a function of HS distance. Bottom right: deviation from FCI dipole, for CCSD and q-UCCSD.

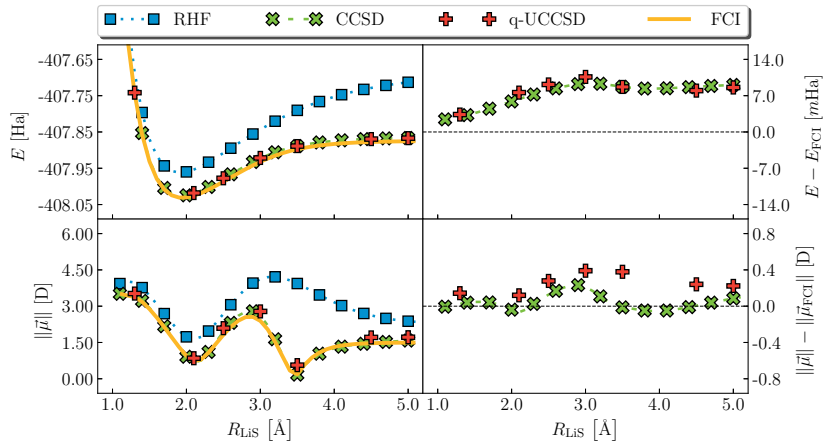


FIG. 6. Calculations for lithium sulfide, Li_2S . Top left: dissociation curve as a function of LiS distance from RHF, CCSD, q-UCCSD and FCI. Top right: deviation from FCI energy, for CCSD and q-UCCSD. Bottom left: norm of the dipole moment as a function of LiS distance. Bottom right: deviation from FCI dipole, for CCSD and q-UCCSD.

3. Lithium hydrogen sulfide (LiSH)

After removing core orbitals, lithium hydrogen sulfide (LiSH) is represented by MOs with $3s$, $3p_x$, $3p_y$, and $3p_z$ character for sulfur, $1s$ character for hydrogen and $2s$, $2p_x$, $2p_y$, $2p_z$, character for lithium, for a total of 18 spin orbitals and 8 electrons. After employing tapering and qubit reductions possible due to symmetry^{37,74}, the ground state energy and dipole moment norms were calculated on the simulator with 15 qubits.

Results are shown in Figures 4 and 5. In Figure 4, the dissociation of the LiS bond is studied by varying R_{LiS} with all other internal coordinates fixed at their experimental values⁷⁵. For all but the largest values of R_{LiS} , CCSD is in better agreement with FCI for both the energy and the dipole moment norm. As in the H_2S case, the most challenging regime is the intermediate dissociation region, where the q-UCCSD energy is overestimated by 5 milliHartrees and the dipole moment norm by $\sim 20\%$ at $R_{\text{LiS}} \simeq 2.7 \text{ \AA}$. Note that, just as for H_2S , at large R_{LiS} , the dipole moment norm converges towards $\|\vec{\mu}\| \simeq 0.67 \text{ D}$, the dipole moment of the HS fragment.

A very different situation is seen for the dissociation of the SH bond, illustrated in Figure 5. Description of the dissociation regime is more challenging for both CC flavors than that seen for the breaking of the Li-S bond, with q-UCCSD again performing better at large bond length. The FCI dipole moment norm decreases monotonically with R_{SH} , a trend that both CC flavors reproduce qualitatively, but not quantitatively, particularly at longer bond lengths. Note that, in the large R_{SH} regime, CCSD and q-UCCSD dipole norms converge towards $\|\vec{\mu}\| \simeq 2.10 \text{ D}$, which is higher than the FCI value (1.52 D), signaling the limited accuracy of the underlying Ansatz.

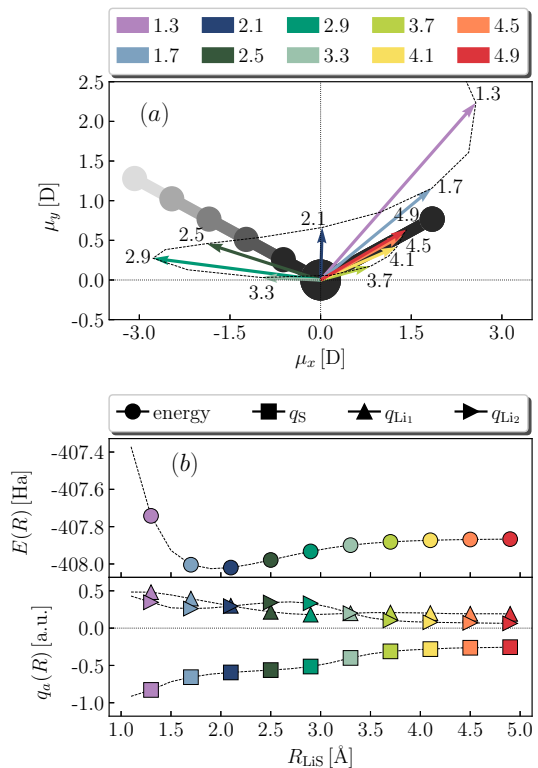


FIG. 7. (a) Evolution of the dipole moment vector of LiS along breaking of the LiS bond. The length of the arrow is the dipole moment norm, shown in Figure 6. The black circles in the background denote the S (large) and fixed Li (small) atom, and the moving gray circles illustrate the departing Li atom. (b) Evolution of energy (top) and partial charges (bottom) of LiS along breaking of the LiS bond. Colors correspond to different bondlengths, dotted black lines are a guide for the eye, illustrating the evolution of dipole vector, energy and charges with bondlength.

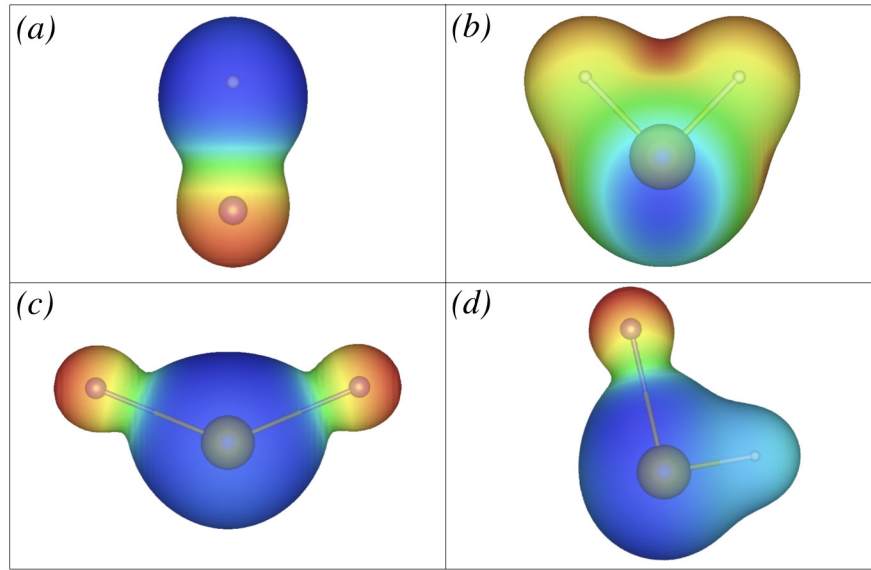


FIG. 8. Contour plots of the q-UCCSD molecular electrostatic potential of LiH, H₂S, Li₂S and LiSH (a,b,c,d respectively) at equilibrium geometry. Contour plots are shown along the isosurfaces of the q-UCCSD charge density with values 0.025, 0.02, 0.025 and 0.025 respectively. Molecular electrostatic potential values range between minimum values -0.05, -0.04, -0.02, -0.04 (blue) and maximum values 0.60, 0.12, 0.53, 0.53 (red) respectively. White, purple and yellow spheres represent H, Li and S atoms respectively.

component	unit	LiH		H ₂ S		LiSH		Li ₂ S	
		q-UCCSD	FCI	q-UCCSD	FCI	q-UCCSD	FCI	q-UCCSD	FCI
Q_{10}	D	-1.8286	-1.8286	0.3520	0.3518	0.9445	0.8079	0.3341	0.2853
Q_{11c}	D					0.1159	0.1154		
Q_{20}	D Å	-5.0908	-5.0908	-8.8799	-8.8805	-6.0715	-6.5529	-15.3387	-15.4943
Q_{21c}	D Å					-1.3555	-1.3962		
Q_{22c}	D Å			0.7224	0.7224	1.4482	1.4910	8.8109	8.5606
Q_{30}	D Å ²	-17.6025	-17.6026	-3.0819	-3.0828	-20.3586	-17.6287	-11.1787	-11.8992
Q_{31c}	D Å ²					5.3521	5.5159		
Q_{32c}	D Å ²			-0.2627	-0.2634	-3.5015	-3.6918	17.3761	17.0057
Q_{33c}	D Å ²					-0.8122	-0.8108		
Q_{33s}	D Å ²					-0.0664	-0.0661		
Q_{40}	D Å ³	-77.1731	-77.1730	-48.7331	-48.7366	-91.8761	-105.8862	-169.7058	-173.6052
Q_{41c}	D Å ³					-6.5822	-7.4223		
Q_{42c}	D Å ³			-1.9550	-1.9565	15.1501	16.1430	-26.5829	-29.2577
Q_{43c}	D Å ³					-9.4300	-9.3020		
Q_{43s}	D Å ³					-0.3018	-0.2849		
Q_{44c}	D Å ³			0.1150	0.1146	0.8223	0.8661	68.6044	68.6344
Q_{44s}	D Å ³					-2.7937	-2.8335		

TABLE I. Multipole moments for LiH, H₂S, LiSH and Li₂S (top to bottom) in traceless spherical Buckingham form, at equilibrium geometry, in the center of mass frame. Blank entries correspond to multipole moments that are exactly zero due to the symmetry.

4. Lithium sulfide (Li₂S)

After removal of the core orbitals for lithium and sulfur, lithium sulfide Li₂S is represented by MOs with 3s, 3p_x, 3p_y, 3p_z character for sulfur and 2s, 2p_x, 2p_y, 2p_z character for lithium, for a total of 24 spin orbitals and 8 electrons. After employing tapering and qubit reductions to account for molecular symmetries, the ground state energy and dipole moment norms were calculated on the simulator with 21 qubits. q-

UCCSD and CCSD estimates for energy and dipole are similar in accuracy along bond stretching.

Results are given in Figure 6. Interestingly, we observe that the norm of the dipole moment varies non-trivially with R_{LiS} for both CCSD, q-UCCSD, and FCI: it decreases up to $R_{\text{LiS}} \simeq 2.1$ Å, then increases until $R_{\text{LiS}} \simeq 3.0$ Å, then decreases until $R_{\text{LiS}} \simeq 3.5$ Å, and then increases again towards an asymptotic value. For q-UCCSD and FCI, this asymptotic value is of $\|\vec{\mu}\| \simeq 1.72$ D and 1.49 D respectively.

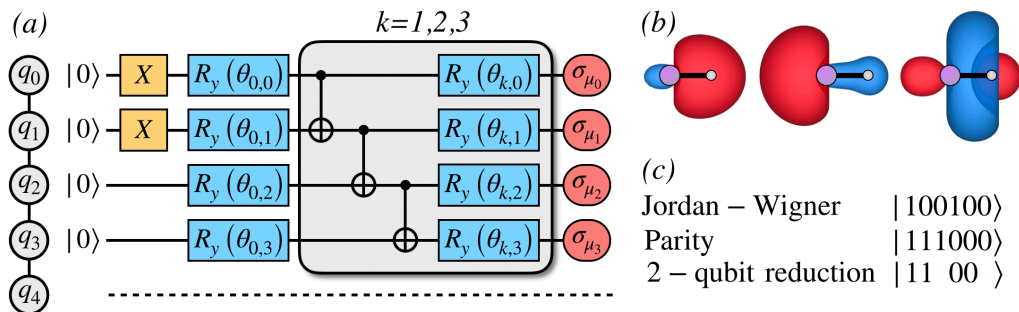


FIG. 9. (a) Schematic representation of the 5-qubit linearly-connected devices employed in this work, and of the quantum circuit used to simulate the ground-state energy and dipole moment of LiH. Orange symbols denote gates encoding of the Hartree-Fock state, blue symbols the y -rotations defining the variational Ansatz, and red symbols the measurements of Pauli operators. (b) Molecular orbitals (MO) encoded on the quantum hardware, for LiH at equilibrium geometry, respectively the highest occupied MO and the two virtual MOs in the A_1 irreducible representation of the $C_{\infty v}$ group (left to right). (c) Binary strings encoding the Hartree-Fock wavefunction under Jordan-Wigner and parity mappings, without and with removal of the two qubits related to the spin-up and spin-down particle number conservation in the parity mapping (top to bottom).

This behavior is elucidated in Figure 7, where we consider the evolution of the dipole vector of Li_2S along breaking of a single LiS bond. As the bond length evolves from 1.3 to 2.1 Å (equilibrium), the dipole moment decreases in length, and rotates towards the bisector of the Li-S-Li triangle.

As the bondlength further increases, the dipole moment increases again in length, rotating towards the departing Li atom, until the point of inflection of the potential energy curve ($R_{\text{LiS}} \simeq 3.0$ Å) is reached. There, at q-UCCSD level, it suddenly rotates towards the unbroken LiS bond. Note that FCI values for the dipole moment of LiSH at long SH distance are very close to those of Li_2S at long LiS distance (1.52 and 1.49 Debye respectively), since they both result in a fragment of LiS.

D. Study of electrostatic properties

In this section, we evaluate multipole moments, charge densities and electrostatic potentials for the species discussed in the previous section, focusing on equilibrium geometries.

In Figure 8, we evaluate charge densities and molecular electrostatic potentials. The contour plots qualitatively illustrate the electronegative nature of sulfur, which hosts negative partial charges in compounds (b,c,d). On the other hand, as expected, lithium has low electronegativity and hosts positive partial charges in compounds (a,c,d).

In Table I, we list the multipole moments for LiH, H_2S , LiSH and Li_2S respectively. The comparison between q-UCCSD and FCI demonstrate the accuracy of the former: higher multipole moments, which are notoriously very sensitive physical quantities to the choice of method, exhibit somewhat large deviations. Such a limited accuracy is also a reflection of the heuristic nature of the q-UCCSD Ansatz, and pinpoints the need of developing more accurate Ansätze and methodologies, in order to satisfactorily describe sensitive electrostatic properties of molecules.

We note that molecular electrostatic potentials can be used

to obtain partial charges through the restrained electrostatic potential (RESP) technique^{76–79}, offering further insight into the interaction between molecules and their dissociation. For example, in Figure 7, we show the partial charges of Li_2S along breaking of the LiS bond: the Li atom departing from the molecule is neutral in the large R_{LiS} limit, while the remaining Li and S atoms carry partial charges responsible for the asymptotic value of the dipole moment.

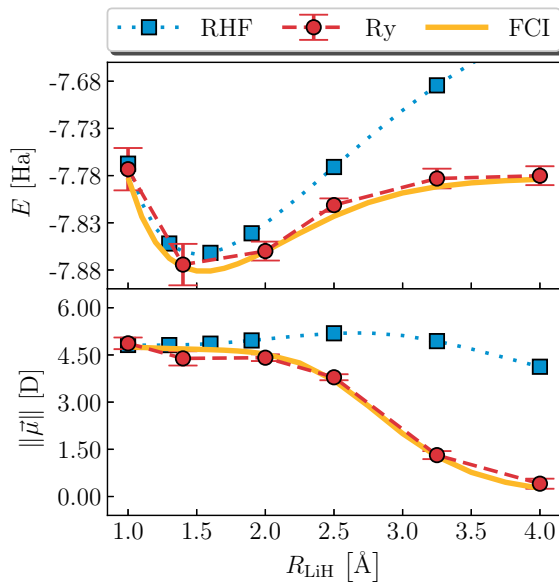


FIG. 10. Hardware results of ground-state energy (top) and dipole moment (bottom) calculations for LiH on the 5 qubit devices accessed via IBM Quantum Experience. (Top: energy in Hartrees as a function of interatomic distance, in Angstroms.

E. Quantum chemistry calculations on quantum devices

Next, the dipole moment of lithium hydride was evaluated using quantum hardware as sketched in Figure 9. We employ the hardware-efficient R_y Ansatz to estimate the ground-state energy and dipole moment at representative values of R_{LiH} . We used a circuit with cNOT entangling gates with linear connectivity and 3 layers as illustrated in Figure 9.

To the best of our knowledge, these are the first evaluations of dipole moments on quantum hardware.

We chose to study six bond lengths representative of the polar and dissociation regimes. We chose the R_y Ansatz because experience²⁰ suggests that, for small molecules like LiH, it can deliver accurate ground state energies with modest quantum resources, unlike q-UCCSD.

Results from hardware experiments in presence of readout error mitigation are shown. A Richardson extrapolation^{69,70} is also conducted, with the aim of further mitigating the impact of noise (intermediate data are listed in the Supplementary Material). As seen in Figure 10, the qualitative behavior of both energies and dipoles is correctly captured by the hardware experiments upon extrapolation. In particular, the dipole moment is accurate within $\sim 10\%$ in the polar regime. Future research will explore approaches to improve these results quantitatively, for example by the use of circuits with higher depth, by the exploration of multiple Ansätze or by the use of different error mitigation techniques.

CONCLUSIONS

Herein, we have reported on the simulations of four molecules (LiH, H₂S, LiSH and Li₂S) that increase in complexity to Li₂S which is relevant to the study of lithium-sulfur batteries. We showed that we could obtain ground state energies for LiH and H₂S within 1 mHa from FCI. For species with more valence electrons, our calculations pinpoint the limitations of Ansätze based on single and double electronic excitations, especially away from equilibrium.

Differences could be observed in the LiSH molecule, depending on whether the hydrogen or lithium atom was dissociated from the sulfur atom: when the SH bond is dissociated, the dipole moment decreases monotonically towards a large (~ 1.5 D) asymptotic limit, and when the LiS bond is dissociated it converges non-monotonically towards a smaller asymptotic value (0.57 D). The asymptotic values of the dipole moment norms are a reflection of the greater polarity of the LiS bond compared to the SH bond. The non-monotonicity, on the other hand, is analogous to the behavior seen in the Li₂S molecule, which is due to non-trivial changes in the direction of the dipole moment as R_{LiS} changes.

Furthermore, the effects of electronic distribution changes could be observed when evaluating the dipole moment of LiH. Additionally, we showed that the LiH could be qualitatively determined on quantum hardware with 4 qubits. This is a notable demonstration of the capabilities of the hardware since the dipole moment of lithium hydride changes from strongly polarized in its ionic state to effectively neutral at long bond

distances over ~ 2.5 Å, representing a highly entangled state at this distance.

Characterizing the electronic structure of Li-S compounds is an important step towards understanding lithium-sulfur batteries. However, achieving this goal with quantum computers requires further methodological improvements. For example, achieving the ability to tackle larger and more relevant chemical species^{12,13,80} and non-minimal basis sets^{81–83}, developing Ansätze that achieve a balance between hardware efficiency and chemical insights^{27,29,84–86}, and incorporating nuclear motion effects^{87–90}.

Our work provides a stepping stone on the way to larger quantum computing calculations, on polyanions formed upon discharge in the Li-S battery. These calculations will have the potential to compare between radical and ionic mechanisms of the electrochemical reduction of sulfur to lithium sulfide with lithium metal.

SUPPLEMENTARY MATERIAL

See supplementary material for details of both the quantum experiments and the classical simulations, including investigation of the LiH CCSD energy and dipole moment across the dissociation profile using different basis sets.

ACKNOWLEDGMENTS

We are indebted to many colleagues for helpful discussions, particularly Stephen Wood, Panagiotis Barkoutsos and Ivano Tavernelli.

TG, JL, MM and JER acknowledge the IBM Research Cognitive Computing Cluster service for providing resources that have contributed to the research results reported in this paper.

This paper is dedicated to the memory of Prof. Dr. Dr. Andreas Hintennach.

DATA AVAILABILITY

The data that support the findings of this study are available from the corresponding author upon reasonable request.

REFERENCES

- ¹P. Gibot, M. Casas-Cabanas, L. Laffont, S. Levasseur, P. Carlach, S. Hamelet, J.-M. Tarascon, and C. Masquelier, *Nat. Mater* **7**, 741 (2008).
- ²P. G. Bruce, S. A. Freunberger, L. J. Hardwick, and J.-M. Tarascon, *Nat. Mater* **11**, 19 (2012).
- ³M. Wild, L. O’Neill, T. Zhang, R. Purkayastha, G. Minton, M. Marinescu, and G. Offer, *Energy Environ. Sci* **8**, 3477 (2015).
- ⁴M. Hagen, D. Hanselmann, K. Ahlbrecht, R. Maça, D. Gerber, and J. Tübke, *Adv. Energy Mater* **5**, 1401986 (2015).
- ⁵D. Zheng, X. Zhang, J. Wang, D. Qu, X. Yang, and D. Qu, *J. Power Sources* **301**, 312 (2016).
- ⁶R. Fang, S. Zhao, Z. Sun, D.-W. Wang, H.-M. Cheng, and F. Li, *Adv. Mater* **29**, 1606823 (2017).

- ⁷H. Yamin, A. Gorenshstein, J. Penciner, Y. Sternberg, and E. Peled, *J. Electrochem. Soc.* **135**, 1045 (1988).
- ⁸Y. V. Mikhaylik and J. R. Akridge, *J. Electrochem. Soc.* **151**, A1969 (2004).
- ⁹C. Barchasz, F. Molton, C. Duboc, J.-C. Leprêtre, S. Patoux, and F. Alloin, *Anal. Chem.* **84**, 3973 (2012).
- ¹⁰M. Cuisinier, P.-E. Cabelguen, B. Adams, A. Garsuch, M. Balasubramanian, and L. Nazar, *Energy Environ. Sci.* **7**, 2697 (2014).
- ¹¹T. A. Pascal, K. H. Wujcik, J. Velasco-Velez, C. Wu, A. A. Teran, M. Kapilashrami, J. Cabana, J. Guo, M. Salmeron, N. Balsara, *et al.*, *J. Phys. Chem. Lett.* **5**, 1547 (2014).
- ¹²S.-H. Chung, C.-H. Chang, and A. Manthiram, *Adv. Funct. Mater.* **28**, 1801188 (2018).
- ¹³T. Li, X. Bai, U. Gulzar, Y.-J. Bai, C. Capiglia, W. Deng, X. Zhou, Z. Liu, Z. Feng, and R. Proietti Zaccaria, *Adv. Funct. Mater.* **29**, 1901730 (2019).
- ¹⁴K. H. Wujcik, D. R. Wang, A. A. Teran, E. Nasybulin, T. A. Pascal, D. Prendergast, and N. P. Balsara, "Determination of redox reaction mechanisms in lithium-sulfur batteries," in *Electrochemical Engineering* (John Wiley & Sons, Ltd, 2018) Chap. 3, pp. 41–74.
- ¹⁵A. Aspuru-Guzik, A. D. Dutoi, P. J. Love, and M. Head-Gordon, *Science* **309**, 1704 (2005).
- ¹⁶I. M. Georgescu, S. Ashhab, and F. Nori, *Rev. Mod. Phys.* **86**, 153 (2014).
- ¹⁷I. Kassal, J. D. Whitfield, A. Perdomo-Ortiz, M.-H. Yung, and A. Aspuru-Guzik, *Annu. Rev. Phys. Chem.* **62**, 185 (2011).
- ¹⁸Y. Cao, J. Romero, J. P. Olson, M. Degroote, P. D. Johnson, M. Kieferová, I. D. Kivlichan, T. Menke, B. Peropadre, N. P. D. Sawaya, S. Sim, L. Veis, and A. Aspuru-Guzik, *Chem. Rev.* **119**, 10856 (2019).
- ¹⁹A. Peruzzo, J. McClean, P. Shadbolt, M.-H. Yung, X.-Q. Zhou, P. J. Love, A. Aspuru-Guzik, and J. L. O'Brien, *Nat. Commun.* **5**, 4213 (2014).
- ²⁰A. Kandala, A. Mezzacapo, K. Temme, M. Takita, M. Brink, J. M. Chow, and J. M. Gambetta, *Nature* **549**, 242 (2017).
- ²¹P. J. Ollitrault, A. Kandala, C.-F. Chen, P. K. Barkoutsos, A. Mezzacapo, M. Pistoia, S. Sheldon, S. Woerner, J. M. Gambetta, and I. Tavernelli, *Phys. Rev. Research* **2**, 043140 (2020).
- ²²P. J. J. O'Malley, R. Babbush, I. D. Kivlichan, J. Romero, J. R. McClean, R. Barends, J. Kelly, P. Roushan, A. Tranter, N. Ding, B. Campbell, Y. Chen, Z. Chen, B. Chiaro, A. Dunsworth, A. G. Fowler, E. Jeffrey, E. Lucero, A. Megrant, J. Y. Mutus, M. Neeley, C. Neill, C. Quintana, D. Sank, A. Vainsencher, J. Wenner, T. C. White, P. V. Coveney, P. J. Love, H. Neven, A. Aspuru-Guzik, and J. M. Martinis, *Phys. Rev. X* **6**, 031007 (2016).
- ²³J. I. Colless, V. V. Ramasesh, D. Dahlen, M. S. Blok, M. E. Kimchi-Schwartz, J. R. McClean, J. Carter, W. A. de Jong, and I. Siddiqi, *Phys. Rev. X* **8**, 011021 (2018).
- ²⁴Q. Gao, H. Nakamura, T. P. Gujarati, G. O. Jones, J. E. Rice, S. P. Wood, M. Pistoia, J. M. Garcia, and N. Yamamoto, *arXiv:1906.10675* (2019).
- ²⁵B. Bauer, S. Bravyi, M. Motta, and G. Kin-Lic Chan, *Chem. Rev.* **120**, 12685–12717 (2020).
- ²⁶S. McArdle, S. Endo, A. Aspuru-Guzik, S. C. Benjamin, and X. Yuan, *Rev. Mod. Phys.* **92**, 015003 (2020).
- ²⁷H. R. Grimsley, S. E. Economou, E. Barnes, and N. J. Mayhall, *Nat. Commun.* **10**, 1 (2019).
- ²⁸T. Bian, D. Murphy, R. Xia, A. Daskin, and S. Kais, *Mol. Phys.* **117**, 2069 (2019).
- ²⁹Y. Nam, J.-S. Chen, N. C. Pisenti, K. Wright, C. Delaney, D. Maslov, K. R. Brown, S. Allen, J. M. Amini, J. Apisdorf, *et al.*, *npj Quantum Inf.* **6**, 1 (2020).
- ³⁰J. Romero, R. Babbush, J. R. McClean, C. Hempel, P. J. Love, and A. Aspuru-Guzik, *Quantum Sci. Technol.* **4**, 014008 (2018).
- ³¹J. M. Turney, A. C. Simmonett, R. M. Parrish, E. G. Hohenstein, F. A. Evangelista, J. T. Fermann, B. J. Mintz, L. A. Burns, J. J. Wilke, M. L. Abrams, N. J. Russ, M. L. Leininger, C. L. Janssen, E. T. Seidl, W. D. Allen, H. F. Schaefer, R. A. King, E. F. Valeev, C. D. Sherrill, and T. D. Crawford, *Wiley Interdiscip. Rev. Comput. Mol. Sci.* **2**, 556 (2012).
- ³²P. Jordan and E. P. Wigner, in *The Collected Works of Eugene Paul Wigner* (Springer, 1993) pp. 109–129.
- ³³S. B. Bravyi and A. Y. Kitaev, *Ann. Phys.* **298**, 210 (2002).
- ³⁴J. T. Seeley, M. J. Richard, and P. J. Love, *J. Chem. Phys.* **137**, 224109 (2012).
- ³⁵K. Setia and J. D. Whitfield, *J. Chem. Phys.* **148**, 164104 (2018).
- ³⁶F. Verstraete and J. I. Cirac, *J. Stat. Mech.: Theory Exp* **2005**, P09012 (2005).
- ³⁷S. Bravyi, J. M. Gambetta, A. Mezzacapo, and K. Temme, *arXiv preprint arXiv:1701.08213* (2017).
- ³⁸K. Setia, S. Bravyi, A. Mezzacapo, and J. D. Whitfield, *Phys. Rev. Research* **1**, 033033 (2019).
- ³⁹M. Staudtner and S. Wehner, *New J. Phys.* **20**, 063010 (2018).
- ⁴⁰A. J. Stone, *The theory of intermolecular forces*, 2nd ed. (Oxford University Press, 2013).
- ⁴¹A. D. Buckingham, *Chem. Soc. Rev.* **13**, 183 (1959).
- ⁴²A. D. Buckingham, *J. Chem. Phys.* **30**, 1580 (1959).
- ⁴³A. D. Buckingham, "Permanent and induced molecular moments and long-range intermolecular forces," in *Advances in Chemical Physics: Intermolecular Forces*, edited by J. O. Hirschfelder (Wiley Online Library, 1967) Chap. 2, pp. 107–142.
- ⁴⁴C. Gray and B. Lo, *Chem. Phys.* **14**, 73 (1976).
- ⁴⁵G. Fitzgerald, R. J. Harrison, and R. J. Bartlett, *J. Chem. Phys.* **85**, 5143 (1986).
- ⁴⁶J. E. Rice, R. D. Amos, N. C. Handy, T. J. Lee, and H. F. Schaefer III, *J. Chem. Phys.* **85**, 963 (1986).
- ⁴⁷A. C. Scheiner, G. E. Scuseria, J. E. Rice, T. J. Lee, and H. F. Schaefer III, *J. Chem. Phys.* **87**, 5361 (1987).
- ⁴⁸E. Salter, G. W. Trucks, and R. J. Bartlett, *J. Chem. Phys.* **90**, 1752 (1989).
- ⁴⁹J. Gauss, J. F. Stanton, and R. J. Bartlett, *J. Chem. Phys.* **95**, 2639 (1991).
- ⁵⁰J. Gauss, J. F. Stanton, and R. J. Bartlett, *J. Chem. Phys.* **95**, 2623 (1991).
- ⁵¹L. Lodi, R. N. Tolchenov, J. Tennyson, A. Lynas-Gray, S. V. Shirin, N. F. Zobov, O. L. Polyansky, A. G. Császár, J. N. Van Stralen, and L. Visscher, *J. Chem. Phys.* **128**, 044304 (2008).
- ⁵²I. Kassal and A. Aspuru-Guzik, *J. Chem. Phys.* **131**, 224102 (2009).
- ⁵³K. Mitarai, Y. O. Nakagawa, and W. Mizukami, *Phys. Rev. Research* **2**, 013129 (2020).
- ⁵⁴T. E. O'Brien, B. Senjean, R. Sagastizabal, X. Bonet-Monroig, A. Dutkiewicz, F. Buda, L. DiCarlo, and L. Visscher, *npj Quantum Inf.* **5**, 1 (2019).
- ⁵⁵I. O. Sokolov, P. K. Barkoutsos, L. Moeller, P. Suchsland, G. Mazzola, and I. Tavernelli, *arXiv preprint arXiv:2008.08144* (2020).
- ⁵⁶R. M. Parrish, E. G. Hohenstein, P. L. McMahon, and T. J. Martinez, *arXiv preprint arXiv:1906.08728* (2019).
- ⁵⁷G. Aleksandrowicz, T. Alexander, P. Barkoutsos, L. Bello, Y. Ben-Haim, D. Bucher, F. Cabrera-Hernández, J. Carballo-Franquis, A. Chen, C. Chen, *et al.*, *Zenodo* **16** (2019).
- ⁵⁸W. Kutzelnigg, *J. Chem. Phys.* **77**, 3081 (1982).
- ⁵⁹W. Kutzelnigg and S. Koch, *J. Chem. Phys.* **79**, 4315 (1983).
- ⁶⁰W. Kutzelnigg, *J. Chem. Phys.* **82**, 4166 (1985).
- ⁶¹P. K. Barkoutsos, J. F. Gonthier, I. Sokolov, N. Moll, G. Salis, A. Fuhrer, M. Ganzhorn, D. J. Egger, M. Troyer, A. Mezzacapo, S. Filipp, and I. Tavernelli, *Phys. Rev. A* **98**, 022322 (2018).
- ⁶²C. Zhu, R. H. Byrd, P. Lu, and J. Nocedal, *ACM Trans. Math. Softw.* **23**, 550–560 (1997).
- ⁶³R. H. Byrd, P. Lu, J. Nocedal, and C. Zhu, *SIAM J. Sci. Comput.* **16**, 1190 (1995).
- ⁶⁴J. L. Morales and J. Nocedal, *ACM Trans. Math. Softw.* **38**, 7 (2011).
- ⁶⁵J. C. Spall, *Johns Hopkins APL Tech. Dig.* **19**, 482 (1998).
- ⁶⁶J. C. Spall, in *Proc. IEEE Conf. Decis. Control*, Vol. 4 (1998) pp. 3872–3879.
- ⁶⁷A. W. Cross, L. S. Bishop, S. Sheldon, P. D. Nation, and J. M. Gambetta, *Phys. Rev. A* **100**, 032328 (2019).
- ⁶⁸*ibmq_athens* v1.3.1, *ibmq_bogota* v1.3.1, *ibmq_rome* v1.3.3, and *ibmq_santiago* v1.2.1, IBM Quantum Team, Retrieved from <https://quantum-computing.ibm.com> (2020).
- ⁶⁹K. Temme, S. Bravyi, and J. M. Gambetta, *Phys. Rev. Lett.* **119**, 180509 (2017).
- ⁷⁰A. Kandala, K. Temme, A. D. Córcoles, A. Mezzacapo, J. M. Chow, and J. M. Gambetta, *Nature* **567**, 491 (2019).
- ⁷¹S. Bravyi, S. Sheldon, A. Kandala, D. C. McKay, and J. M. Gambetta, *arXiv:2006.14044* (2020).
- ⁷²E. F. Dumitrescu, A. J. McCaskey, G. Hagen, G. R. Jansen, T. D. Morris, T. Papenbrock, R. C. Pooser, D. J. Dean, and P. Lougovski, *Phys. Rev. Lett.* **120**, 210501 (2018).

- ⁷³N. Stamatopoulos, D. J. Egger, Y. Sun, C. Zoufal, R. Iten, N. Shen, and S. Woerner, *Quantum* **4**, 291 (2020).
- ⁷⁴K. Setia, R. Chen, J. E. Rice, A. Mezzacapo, M. Pistoia, and J. D. Whitfield, *J. Chem. Theory Comput* **16**, 6091 (2020).
- ⁷⁵R. D. Johnson III, *NIST Computational Chemistry Comparison and Benchmark Database, NIST Standard Reference Database Number 101*, Tech. Rep. (NIST, 2020).
- ⁷⁶C. I. Bayly, P. Cieplak, W. D. Cornell, and P. A. Kollman, *J. Phys. Chem* **97**, 10269 (1993).
- ⁷⁷W. D. Cornell, P. Cieplak, C. I. Bayly, and P. A. Kollman, *J. Am. Chem. Soc* **115**, 9620 (2002).
- ⁷⁸P. Cieplak, W. D. Cornell, C. I. Bayly, and P. A. Kollman, *J. Comput. Chem* **16**, 1357 (1995).
- ⁷⁹T. Fox and P. A. Kollman, *J. Phys. Chem. B* **102**, 8070 (1998).
- ⁸⁰A. Manthiram, Y. Fu, S.-H. Chung, C. Zu, and Y.-S. Su, *Chem. Rev* **114**, 11751 (2014).
- ⁸¹T. H. Dunning Jr, *J. Chem. Phys* **90**, 1007 (1989).
- ⁸²D. E. Woon and T. H. Dunning Jr, *J. Chem. Phys* **98**, 1358 (1993).
- ⁸³T. H. Dunning Jr, K. A. Peterson, and A. K. Wilson, *J. Chem. Phys* **114**, 9244 (2001).
- ⁸⁴A. J. McCaskey, Z. P. Parks, J. Jakowski, S. V. Moore, T. D. Morris, T. S. Humble, and R. C. Pooser, *npj Quantum Inf* **5**, 1 (2019).
- ⁸⁵T. Takeshita, N. C. Rubin, Z. Jiang, E. Lee, R. Babbush, and J. R. McClean, *Phys. Rev. X* **10**, 011004 (2020).
- ⁸⁶M. Motta, T. P. Gujarati, J. E. Rice, A. Kumar, C. Masteran, J. A. Latone, E. Lee, E. F. Valeev, and T. Y. Takeshita, *Phys. Chem. Chem. Phys* **22**, 24270 (2020).
- ⁸⁷P. J. Ollitrault, A. Baiardi, M. Reiher, and I. Tavernelli, *Chem. Sci* **11**, 6842 (2020).
- ⁸⁸S. T. Stober, S. M. Harwood, D. Greenberg, T. P. Gujarati, S. Mostame, S. Raman, and D. Trenev, *arXiv preprint arXiv:2003.02303* (2020).
- ⁸⁹N. P. Sawaya, T. Menke, T. H. Kyaw, S. Johri, A. Aspuru-Guzik, and G. G. Guerreschi, *npj Quantum Inf* **6**, 1 (2020).
- ⁹⁰N. P. Sawaya, F. Paesani, and D. P. Tabor, *arXiv preprint arXiv:2009.05066* (2020).